Catal Lett (2008) 125:160–167
DOI 10.1007/s10562-008-9540-3

Structure-activity Relation of Fe_2O_3–CeO_2 Composite Catalysts in CO Oxidation

Huizhi Bao · Xin Chen · Jun Fang · Zhiquan Jiang · Weixin Huang

Received: 1 April 2008 / Accepted: 5 June 2008 / Published online: 24 June 2008

Abstract A series of Fe_2O_3–CeO_2 composite catalysts were synthesized by coprecipitation and characterized by X-ray diffraction (XRD), BET surface area measurement, Raman spectroscopy, and X-ray photoelectron spectroscopy (XPS). Their catalytic activities in CO oxidation were also tested. The Fe_2O_3–CeO_2 composites with an Fe molar percentage below 0.3 form solid solutions with the CeO_2 cubic fluorite structure, in which the doped Fe^{3+} initially substitutes Ce^{4+} in fluorite cubic CeO_2, but then mostly locate in the interstitial sites after a critical concentration of doped Fe^{3+}. With an Fe molar percentage between 0.3 and 0.95, the Fe_2O_3–CeO_2 composites are mixed oxides of the cubic fluorite CeO_2 solid solution and the hematite Fe_2O_3. XPS results indicate that CeO_2 is enriched in the surface region of Fe_2O_3–CeO_2 composites. The Fe_2O_3–CeO_2 composites have much higher catalytic activities in CO oxidation than the individual pure CeO_2 and Fe_2O_3, and the $Fe_{0.1}Ce_{0.9}$ composite shows the best catalytic performance. The structure-activity relation of the Fe_2O_3–CeO_2 composites in CO oxidation is discussed in terms of the formation of solid solution and surface oxygen vacancies. Our results demonstrate a proportional relation between the catalytic activity of cubic CeO_2-like solid solutions and their density of oxygen vacancies, which directly proves the formation of oxygen vacancies as the key step in CO oxidation over oxide catalysts.

H. Bao · X. Chen · J. Fang · Z. Jiang · W. Huang (✉)
Hefei National Laboratory for Physical Sciences at the Microscale and Department of Chemical Physics, University of Science and Technology of China, Hefei 230026, China
e-mail: huangwx@ustc.edu.cn

Keywords Structure-activity relation · CeO_2 · Fe_2O_3 · Oxide solid solution · CO oxidation

1 Introduction

CeO_2 has important and wide applications in heterogeneous catalysis [1–3]. Supported CeO_2 and CeO_2-based mixed oxides are effective catalysts for oxidation of different hydrocarbons [4, 5], for the wet oxidation process of organic compounds in the industrial waste waters, for the removal of total organic carbon from polluted waters from different sources [6, 7]. CeO_2 is also a key promoter in the commercial catalyst used for reducing CO, hydrocarbons, and NO_x emissions from gasoline engines [8, 9]. The wide application of CeO_2 in heterogeneous catalysis is mainly due to two features of CeO_2: the redox couple of Ce(IV)/Ce(III) and the high oxygen storage capacity (OSC) [10]. In the commercial three-way catalyst to reduce CO, hydrocarbons, and NO_x emissions from gasoline engines, CeO_2 acts as an oxygen storage/release medium that is continuously reduced and oxidized under cycling feedstream conditions, in which a complex series of redox reactions occurs on the ceria surface in the presence of lean/rich gas mixtures, involving continuous formation and annihilation of oxygen vacancies and changes in the redox state of Ce(IV)/Ce(III) [1].

Despite its widespread applications, the use of pure CeO_2 is highly discouraged because it is poorly thermally stable and undergoes rapid sintering at high temperatures, thus greatly decreasing its crucial oxygen storage capacity [3, 11, 12]. A general method to increase the thermal stability and OSC of CeO_2 during operations is to introduce other metal ions into the ceria cubic fluorite structure [2, 3, 13–31]. This approach offers an opportunity not only to

improve the performance of the involved metal oxide but also to form new stable compounds that lead to totally different physical and chemical properties. For example, doping ceria with trivalent ions (Pr^{3+} and Tb^{3+}) was reported to lower the activation energy of oxygen release [17], and doping ceria with smaller homovalent Zr^{4+} could obviously enhance its OSC [13]. Fe–Ce mixed oxides has received some attentions because iron oxides and ceria are both of great importance in catalysis. No solid solubility was detected for Fe^{3+}-doped ceria sintered at 1,473 K [21, 22], indicating the difficulty of the dissolution of Fe^{3+} into the ceria lattice by the traditional method. However, Li et al. successfully developed a low-temperature approach (hydrothermal route) to synthesize $Ce_{1-x}Fe_xO_2$ solid solutions with the extremely low oxygen vacancy concentration and the absence of Ce^{3+}, which was attributed to the distribution of Fe^{3+} at Ce^{4+} and interstitial sites according to a ratio of ca. 3:1 [23]. Fe–Ce mixed oxides have also been investigated as the catalysts for wet air oxidation of *p*-coumaric acid [24] and synthesis of 3-pentanone from 1-propanol [25]. Recently Pérez-Alonso et al. synthesized a series of Fe–Ce mixed oxides (100, 95, 85, 50 and 0 at. % Fe metal (Ce balance)) by coprecipitation and investigated their catalytic performance in Fisher-Tropsch synthesis and N_2O decomposition [26, 27]. It was found that the Fe–Ce mixed oxides can form hematite-like and cubic ceria-like solid solutions which show better catalytic performance than the pure metal oxide counterparts [26, 27].

In this paper, we systematically synthesized a series of Fe_2O_3–CeO_2 composites with the Fe atomic ratio (Ce balance) varying from 100% to 0. Their structures were characterized by means of X-ray diffraction (XRD), BET surface area measurement, Raman spectroscopy, and X-ray photoelectron spectroscopy (XPS). The catalytic performance of Fe_2O_3–CeO_2 composites in CO oxidation was also tested. It is generally accepted that CO oxidation under stationary conditions over ceria follows the Mars-van Krevelen-type mechanism, where reaction involves alternate reduction and oxidation of the oxide surface with formation of surface oxygen vacancies (as the key step) and their replenishment by gas-phase oxygen [2], therefore, CO oxidation has been frequently employed as a probe reaction over ceria-contained materials to evaluate different catalyst formulations and investigate mechanistic issues [2, 15, 32–35]. In our study, we find that the Fe_2O_3–CeO_2 composites have much higher catalytic activity in CO oxidation than the individual pure CeO_2 and Fe_2O_3, and the $Fe_{0.1}Ce_{0.9}$ composite shows the best catalytic performance. The structure-activity relation of the Fe_2O_3–CeO_2 composites in CO oxidation is discussed in terms of the formation of solid solution and surface oxygen vacancies.

2 Experimental Section

2.1 Catalyst Preparation

A series of Fe_2O_3–CeO_2 composite catalysts with 100, 95, 90, 80, 70, 60, 50, 40, 30, 20,10, 5, and 0 at. % Fe metal (Ce balance) was synthesized by coprecipitation using urea as the precipitation agent. The calculated amounts of $Fe(NO_3)_3 \cdot 9H_2O$ (Sinopharm Chemical Reagent Co., Ltd, $\geq$ 98.5%) and $(NH_4)_2Ce(NO_3)_6$ (Sinopharm Chemical Reagent Co., Ltd, $\geq$ 99%), and 19.2 g urea (Sinopharm Chemical Reagent Co., Ltd, $\geq$ 99%) were dissolved in 160 mL distilled water. The aqueous solution was refluxed for 8 h at the boiling temperature and then aged overnight at room temperature. Then the precipitates were filtered and washed several times with hot water, dried in vacuum at 353 K for 16 h, and finally calcined under ambient air at 923 K for 8 h. The various Fe_2O_3–CeO_2 composites were referred to as FeACeB, in which A (Fe/(Fe + Ce)) and B (Ce/(Fe + Ce)) are the molar percentage of Fe and Ce, respectively.

2.2 Catalyst Characterization

BET surface areas were acquired on a Beckman Coulter SA3100 Surface Area Analyzer, in which the sample was degassed at 120 °C for 30 min in the nitrogen atmosphere prior to the measurement. Powder X-ray diffraction (XRD) patterns were recorded on a Philips X'Pert PROS diffractometer using a nickel-filtered Cu Kα (0.15418 nm) radiation source, and the operation voltage and operation current are 40 kV and 50 mA, respectively. Raman spectra were obtained in back-scattering configuration on a LA-BRAM-HR Confocal Laser Raman Spectrometer using the visible Ar^+ laser (514.5 nm) as the excitation laser at the ambient condition. The time of acquisition was 30 s. X-ray photoelectron spectroscopy (XPS) measurements were performed on an ESCALAB 250 high performance electron spectrometer using Mg Kα (hv = 1253.6 eV) as the excitation source. The likely charging of the oxide samples was corrected by setting the binding energy of the adventitious carbon (C 1s) to 284.6 eV [36].

2.3 Catalytic Activity Measurements

The catalytic activity of Fe_2O_3–CeO_2 composite catalysts were evaluated with a fixed-bed flow reactor. 50 mg catalyst (particle size: 280–450 μm) was used and the reaction gas consisting of 1% CO and 99% dry air was fed at a rate of 20 mL/min. The composition of the effluent gas was detected with an online GC-14C gas chromatograph equipped with a TDX-01 column (T = 80 C, H_2 as the carrier gas at 30 mL/min). The conversion of CO was

calculated from the change in CO concentrations in the inlet and outlet gases.

3 Results and Discussion

Figure 1 shows XRD patterns of various Fe_2O_3–CeO_2 composites. The pure CeO_2 displays a typical XRD pattern of cubic CeO_2 (fluoride structure) and the pure Fe_2O_3 displays a typical XRD pattern of hematite, α-Fe_2O_3 (hexagonal). The Fe_2O_3–CeO_2 composites with an Fe molar percentage (Fe%) up to 30% only display the typical XRD pattern of cubic CeO_2. The absence of Fe_2O_3-related XRD diffraction peaks in these Fe_2O_3–CeO_2 composites might be due to two factors: (1) Fe_2O_3 forms very fine particles beyond the detection limit of XRD; (2) Fe_2O_3–CeO_2 forms the solid solution with a cubic CeO_2 structure. The formation of Fe–Ce oxide solid solution has been reported to depend on the preparation method, particularly on the final calcinations temperature. Calcining Fe^{3+}-doped ceria at 1,473 K could not form the solid solution [21, 22] whereas a low-temperature hydrothermal approach successfully prepared $Ce_{1-x}Fe_xO_2$ solid solutions [23]. Pérez-Alonso et al. studied the effect of calcinations temperature on the structure of Fe50Ce50 mixed oxides prepared by coprecipitation, in which Fe50Ce50 formed a solid solution upon calcinations at 573 K whereas Fe segregated from the solid solution and formed hematite when the calcinations temperature increased to 773 K and 973 K [26]. Therefore, Fe–Ce oxide solid solution with a cubic CeO_2 structure seems to be thermodynamically mesostable, and at elevated temperatures, Fe in the CeO_2 lattice will segregate and form thermodynamically more stable hematite. When the Fe% in Fe_2O_3–CeO_2 composites exceeds 30%, the XRD peaks arising from hematite appear and intensify with the increasing Fe%, demonstrating the formation of detectable α-Fe_2O_3 crystallites by XRD. Meanwhile, the XRD diffraction peaks from cubic CeO_2 continuously weaken with the increasing Fe%, but are still visible even in the Fe95Ce5 sample. We calculated the lattice constants of cubic CeO_2 phase on basis of its (111) diffraction peak position in XRD spectra. The results demonstrate that the lattice constants of CeO_2 in Fe_2O_3–CeO_2 composites are generally smaller than that in pure CeO_2, indicating that the lattice contraction of cubic CeO_2 occurs in Fe_2O_3–CeO_2 composites. This observation agrees well with previous results [23–27], evidencing the formation of cubic CeO_2-like Fe_2O_3–CeO_2 solid solution in Fe_2O_3–CeO_2 composites. Because of the smaller size of Fe^{3+} (0.64 Å) [37] than Ce^{4+} (1.01 Å) [1], substitution of Ce^{4+} by Fe^{3+} will result in the lattice contraction of cubic CeO_2.

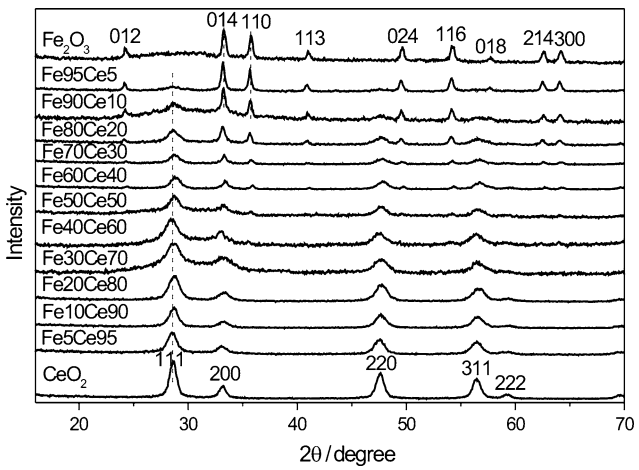

Fig. 1 XRD patterns of various samples

The average crystallite sizes of cubic CeO_2 and hematite in composites were estimated from the corresponding (111) diffraction peak and (110) diffraction peak on basis of the Debye-Scherrer equation, respectively. These results, together with the specific surface areas of the composites, are also shown in Table 1. The crystalline size of cubic CeO2 decreases with the increasing amount of Fe_2O_3 in the composites, however, the crystalline size of hematite does not change much. The specific surface areas of pure CeO_2 and pure Fe_2O_3 are 60 and 34 m^2/g, respectively. Fe5Ce95 and Fe10Ce90 show a similar specific surface area with the pure CeO_2, and other Fe_2O_3–CeO_2 composites show intermediate specific surface areas.

The Raman spectra for samples are shown in Fig. 2. The pure cubic CeO_2 displays an intense band at 463 cm^{-1} assigned to the symmetric breathing mode of the O atoms around each Ce^{4+} that is the single allowed Raman mode with $F_{2\ g}$ symmetry in metal oxides with a fluoride structure [38]. The band intensity at 463 cm^{-1} attenuates with the increasing Fe amount in Fe_2O_3–CeO_2 composites and completely disappears in Fe90Ce10 and Fe95Ce5, which can be accounted for by the decreasing crystalline size of cubic CeO_2, the decreasing Ce amount in composites and the absorption of laser by coexisting Fe(III). The very small size of the crystallites of the oxides can lead to the absence of Raman features [39, 40]. The Raman spectrum of pure Fe_2O_3 corresponds to that of α-Fe_2O_3 [39], exhibiting four bands at 222, 288, 407, and 605 cm^{-1}, respectively. It is noteworthy that the intensity of the Raman bands in pure Fe_2O_3 is much weaker than that in pure CeO2, which can be related to the strong absorbance of hematite at the wavenumber region of the Raman spectrum [37]. This results in a decrease in the sampling depth where the Raman line arises from and accordingly in a loss of the intensity of the Raman bands [41]. The intensity of Raman bands of hematite in composites does not vary much with the decreasing Fe amount, in consistence with the XRD

Table 1 Structural parameters of Fe_2O_3–CeO_2 composites

Samples	Structure	Average crystalline diameter (nm)		BET surface area (m^2/g)
		Cubic CeO_2	Hematite Fe_2O_3	
CeO_2	Cubic CeO_2	11.7		60
Fe5Ce95	Cubic CeO_2	9.3		65
Fe10Ce90	Cubic CeO_2	9.4		57
Fe20Ce80	Cubic CeO_2	8.0		39
Fe30Ce70	Cubic CeO_2	5.7		42
Fe40Ce60	Cubic CeO_2 + hematite Fe_2O_3	6.3		46
Fe50Ce50	Cubic CeO_2 + hematite Fe_2O_3	8.6		42
Fe60Ce40	Cubic CeO_2 + hematite Fe_2O_3	9.0	29.9	44
Fe70Ce30	Cubic CeO_2 + hematite Fe_2O_3	9.0	26.0	46
Fe80Ce20	Cubic CeO_2 + hematite Fe_2O_3	7.7	29.1	46
Fe90Ce10	Cubic CeO_2 + hematite Fe_2O_3	6.1	32.2	41
Fe95Ce5	Cubic CeO_2 + hematite Fe_2O_3	5.1	32.6	45
Fe_2O_3	Hematite Fe_2O_3		29.5	34

result that the crystalline size of hematite does not change much in composites. The Raman bands of hematite disappears when the Fe ratio in composites reaches 0.3 and below, which again is in keeping with the XRD results that the composites with a Fe ratio below 0.4 form the cubic CeO_2-like solid solution.

The pure CeO_2 also display a weak band at 596 cm^{-1}. This feature has been proved to be relevant with oxygen vacancies in CeO_2 [38]. Thus there exist certain an amount of oxygen vacancies in pure CeO_2. The intensity of the band at 596 cm^{-1} initially increases and then decreases with the increasing Fe amount in the composites. As an approach to estimate the concentration of oxygen vacancies in composites, we calculated the intensity ratio of the bands at 596 and 463 cm^{-1} (I_{596}/I_{463}). The results are shown in Fig. 3. With the increasing Fe amount in Fe_2O_3–CeO_2 composites, I_{596}/I_{463} increases and reaches a maximum in Fe10Ce90, then decreases. The band at 596 cm^{-1} disappears when the Fe ratio in composites reaches 0.4 and above. This proves that the doping amount of Fe^{3+} in cubic CeO_2 greatly influences the concentration of oxygen vacancies in Fe_2O_3–CeO_2 composites. Small doping amount of Fe^{3+} facilitates the formation of oxygen vacancies whereas large doping amount of Fe^{3+} annihilates oxygen vacancies. This could be attributed to different doping mechanisms to balance the charge when Ce^{4+} in cubic CeO_2 is substituted by the trivalent M^{3+} cation. One is the vacancy compensation mechanism [17], in which one oxygen vacancy is created to balance the charge when two Ce^{4+} are substituted by two M^{3+}; the other is the dopant interstitial compensation mechanism [1], in which three Ce^{4+} are substituted by three M^{3+} and neutrality is accomplished by the location of one additional Fe^{3+} cation in the interstitial sites of the fluorite cubic CeO_2 structure. The latter mechanism has been claimed to occur in Fe–Ce–O mixed oxides [23, 26], even in Ce-rich Fe–Ce–O mixed oxides [23]. Our results demonstrate that the mechanism of the substitution of Ce^{4+} in CeO_2 by Fe^{3+} depends on the concentration of doped Fe^{3+}. Within the range of low Fe^{3+} concentration, the doping mechanism follows the vacancy compensation mechanism, and thus the concentration of oxygen vacancies increases with the increasing amount of doped Fe^{3+}; however, when the concentration of doped Fe^{3+} exceeds a critical value, the mechanism switches to the dopant interstitial compensation mechanism, in which increasing the amount of doped Fe^{3+} annihilates oxygen vacancies. Therefore, the concentration of oxygen vacancies will exhibit a local maximum with the increasing Fe ratio in Fe_2O_3–CeO_2 composites, as observed in our results. These results also demonstrate that the doped Fe^{3+} initially substitute Ce^{4+} in fluorite cubic CeO_2, but could only locate in the interstitial sites after a critical concentration of doped Fe^{3+}. This could be rationalized by the too large difference between the sizes of Fe^{3+} (0.64 Å) and Ce^{4+} (1.01 Å). Thus it is unlikely for a large amount of Ce^{4+} cations in CeO_2 to be substituted by Fe^{3+} in order to stabilize the fluorite cubic CeO_2 structure. Minervini et al. did theoretical calculations and found that although the vacancy compensation mechanism is energetically favored in the solid solutions formed between trivalent cations and CeO_2, the vacancy compensation mechanism is not so much favored for the smallest trivalent cations such as Ga^{3+}, Cr^{3+}, Al^{3+} or Fe^{3+} as compared to the dopant interstitial compensation mechanism [42].

The surface structure of Fe_2O_3–CeO_2 composites were investigated by XPS. Figure 4 shows the Ce 3d and Fe 2p XPS spectra. The Ce 3d XPS spectra show multiple states arising from different Ce 4f level occupancies in the final state [43]. The labels in Fig. 4 follow the convention established by Burroughs et al. [44], in which U and V

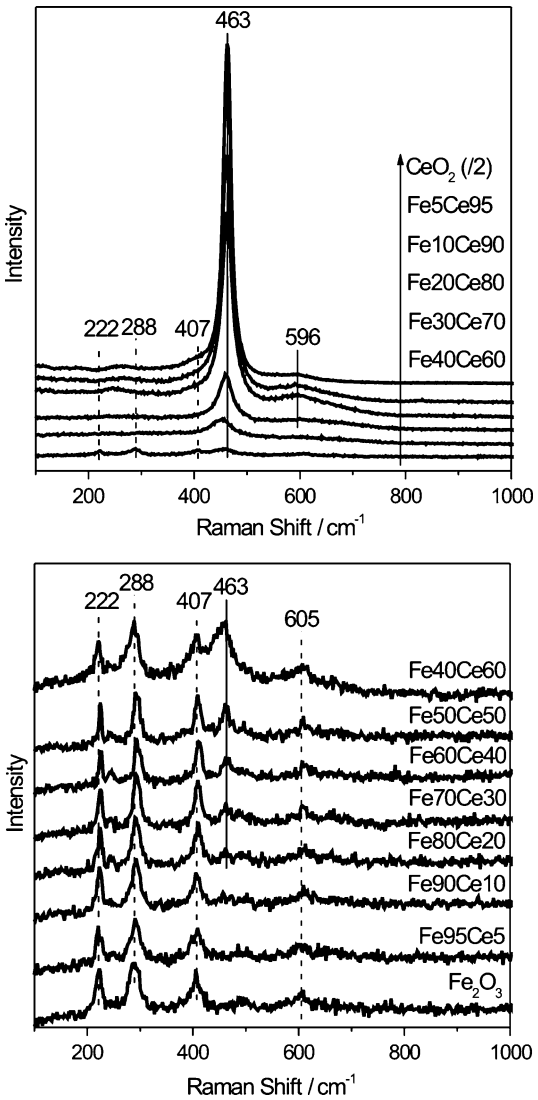

Fig. 2 Raman spectra of various samples

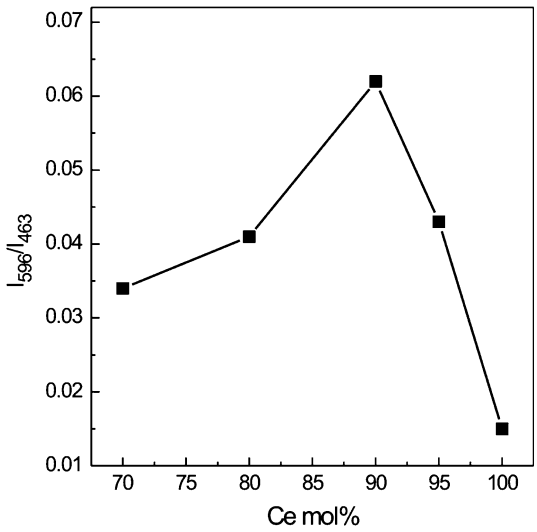

Fig. 3 The I_{596}/I_{463} ratios of CeO_2-like solid solutions calculated from the Raman spectra in Fig. 2

refer to the $3d_{5/2}$ and $3d_{3/2}$ spin-orbital components, respectively. The major difference of the Ce 3d XPS features between Ce(IV) oxide and Ce(III) oxide is that Ce 3d XPS spectrum from Ce(IV) oxide consists of three pairs of spin-orbit doublets whereas that from Ce(III) oxide only two pairs of spin-orbit doublets [44]. The Ce 3d XPS spectrum of the pure CeO_2 shows clear three-pairs of spin-orbital doublets, implying that Ce(IV) dominates in pure CeO_2. But the likely existence of Ce(III) oxide in pure CeO_2 cannot be ruled out because of the overlapping of Ce 3d XPS features of Ce(III) and Ce(IV). The Ce 3d XPS feature is present in all composites, but attenuates with the increasing Fe ratio. Judged from the XPS results, Ce in all Fe_2O_3–CeO_2 composites is mostly Ce(IV).

The Fe5Ce95 and Fe10Ce90 solid solutions do not exhibit Fe 2p feature in the XPS spectra, which implies that Fe in CeO_2-like cubic solid solution mostly locates in the bulk. However, the Fe30Ce70 solid solution shows a quite strong Fe 2p XPS feature. This might be taken as an indicative that Fe^{3+} mostly locates in the interstitial sites of the cubic fluorite structure, consistent with previous Raman results. The Fe 2p XPS feature grows with the increasing Fe ratio in the composites. The binding energy of Fe $2p_{3/2}$ locates at 710.2 eV. The pure Fe_2O_3, Fe95Ce5, and Fe90Ce10 also show a weak peak at 718.1 eV, which is a characteristic shake-up satellite line for Fe(III) species [45]. These results indicate that Fe in Fe_2O_3–CeO_2 composites is mostly Fe(III). Because XPS is a surface-sensitive technique, the XPS results strong demonstrate that the CeO_2-like cubic solid solution is enriched in the surface region of Fe_2O_3–CeO_2 composites.

The O 1s XPS spectra of various samples are shown in Fig. 5. The O 1s XPS spectrum of pure cubic CeO_2 was well fitted by a major component and a shoulder with O 1s binding energies at 528.5 and 530.9 eV. The 528.5 eV peak could be unambiguously assigned to oxygen bound to Ce(IV). Praline et al. previously reported that oxygen attached to Ce(III) showed a binding energy ca. 1–2 eV higher than oxygen attached to Ce(IV) in CeO_2 [46], but a recent work demonstrated that strongly bound surface hydroxyls associated with reduced Ce sites in CeO_2 also exhibit an O 1s peak with a binding energy ca. 1–2 eV higher than that of oxygen attached to Ce(IV) [47]. Thus observance of the O 1s peak at 530.9 eV proves the existence of Ce(III) in pure cubic CeO_2, agreeing with previous Raman spectrum that indicates the existence of oxygen vacancies. The O 1s XPS spectrum of pure hematite shows two components with O 1s binding energies at 529.5, and 531.4 eV, assigned to lattice oxygen in hematite and surface hydroxyls [36]. Because the complicate chemical

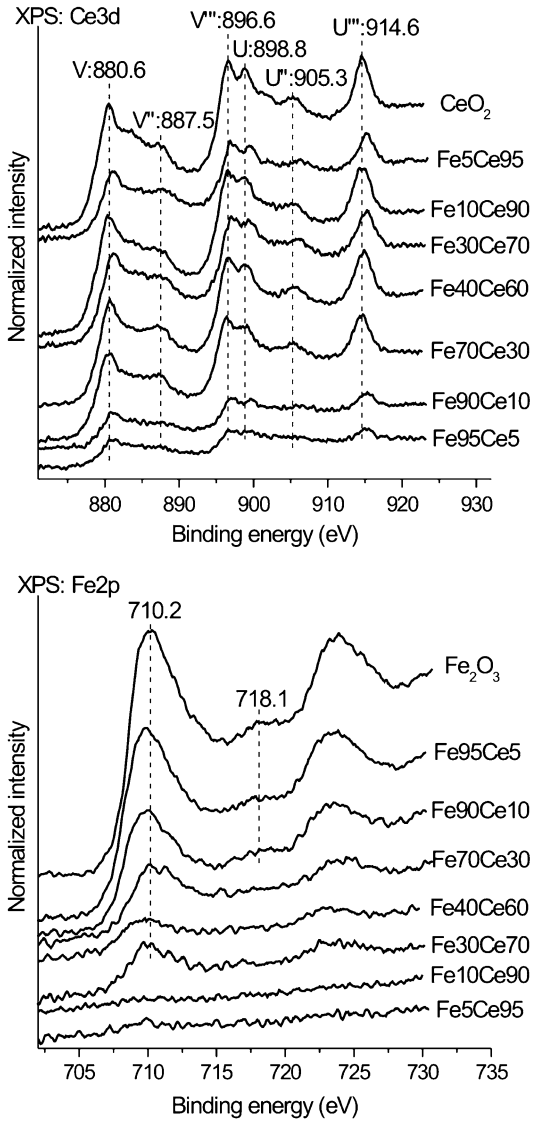

Fig. 4 Normalized Ce 3d and Fe 2p XPS spectra of various samples

environments of O in mixed oxides, we did not fit their O 1s XPS spectra.

The catalytic activities of these composite oxide catalysts in CO oxidation were evaluated. Figure 6a shows the activity of selected samples at different reaction temperatures. Pure CeO_2 and hematite become active in CO oxidation above 500 K and achieve a 100% CO conversion above 700 K. The Fe_2O_3–CeO_2 composites exhibit much better catalytic performances than the individual oxides, and Fe10Ce90 is the best catalyst. The catalytic activity of various catalysts can be more easily compared by their $T_{50\%}$ (the reaction temperature corresponding to a 50% CO conversion), as shown in Fig. 6b. The $T_{50\%}$ for pure cubic CeO_2 is ca. 620 K, and sharply decreases to 517 K for Fe5Ce95 and further decreases to 500 K for Fe10Ce90, and then slowly increases with the further increasing Fe ratio in the composites, but Fe95Ce5 shows a lower $T_{50\%}$ than its neighbors. To understand the structure-activity relation, we calculated the specific rates of the catalysts at 523 K and made a comparison between the specific rates and specific surface areas of the catalysts (right panel of Fig. 7). The specific rate of Fe10Ce90 is about 6 times as that of pure CeO_2, demonstrating the dramatic improvement of the catalytic activity by solid solution formation. However, it is obvious that the change in the specific surface areas of these catalysts cannot adequately account for the observed change in their catalytic activity. For example, Fe5Ce95 has a larger specific surface area than Fe10Ce90, but exhibits a lower specific rate than Fe10Ce90.

The structural characterizations establish that FeACeB ($A \leq 30$) forms a single phase of cubic CeO_2-like solid solution whereas FeACeB ($A \geq 40$) is a mixture of cubic CeO_2-like solid solution and hematite. Thus we focus on the structure-activity of cubic CeO_2-like solid solutions in CO oxidation. The activity of FeACeB ($A \geq 40$) composites should be dominated by the exposed fraction of

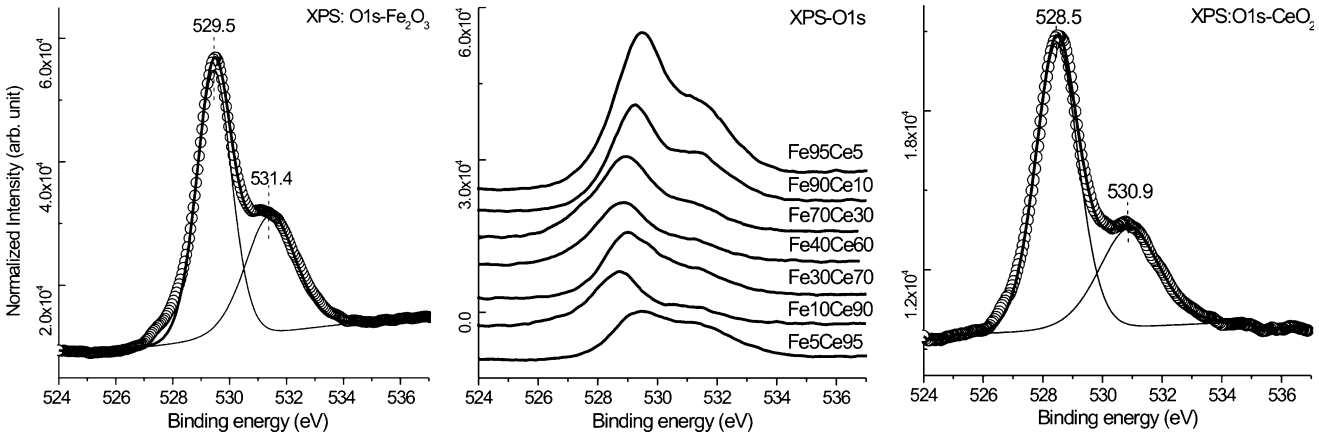

Fig. 5 Normalized O 1s XPS spectra of pure Fe_2O_3 and pure CeO_2 with fitting results (experimental and fitting data in scatter and lines, respectively) and Fe_2O_3–CeO_2 mixed oxides

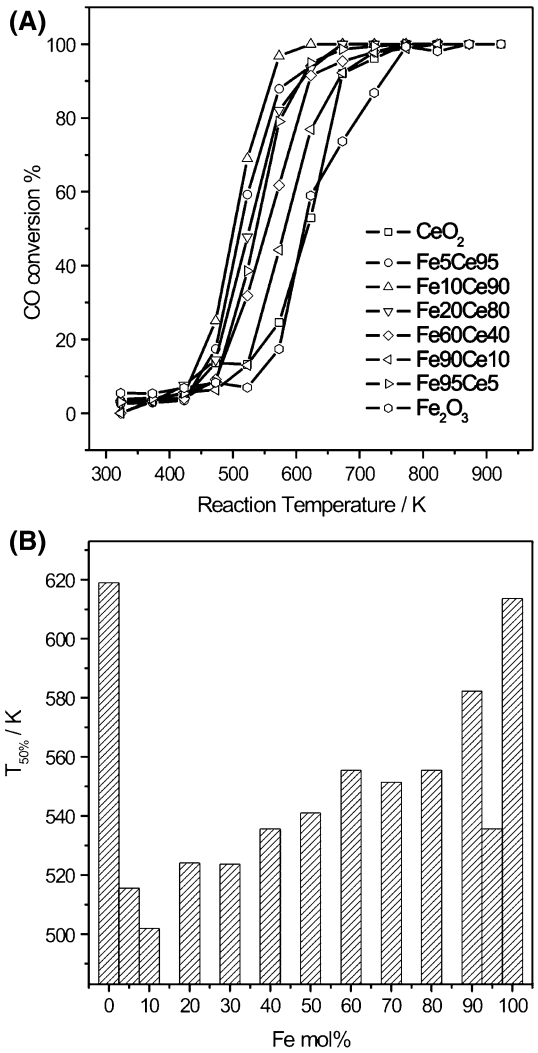

Fig. 6 CO conversion and $T_{50\%}$ of various samples in CO oxidation

cubic CeO_2-like solid solution that, however, could not be determined. It is generally accepted that CO oxidation under stationary conditions over ceria follow a Mars-van Krevelen-type mechanism, where reaction involves alternate reduction and oxidation of the oxide surface with formation of surface oxygen vacancies (as the key step) and their replenishment by gas-phase oxygen. Thus the density of surface oxygen vacancies in the oxide solid solution should play an important role in their catalytic activity in CO oxidation.

As we discussed above, the I_{596}/I_{463} ratio in the Raman spectra represents the relative amount of surface oxygen vacancies in the probed area of cubic CeO_2-like solid solutions. The probed area in Raman spectroscopic measurements was determined by the size of the laser spot and kept unchanged for all samples. Therefore, the density of surface oxygen vacancies of a cubic CeO_2-like solid solution can be approximated by the product between its specific surface area and the I_{596}/I_{463} ratio calculated from its Raman spectrum. We thus calculated the density of surface oxygen vacancies for the solid solutions and plotted the specific rates as a function of the density of surface oxygen vacancies (lower panel of Figure 7). It can be seen that the specific rates of the solid solutions are proportional to their densities of surface oxygen vacancies, demonstrating that the density of surface oxygen vacancies in the CeO_2-like solid solution determines its activity in CO oxidation. This result gives a direct experimental proof that formation of surface oxygen vacancies is the key step in CO oxidation catalyzed by ceria and CO oxidation follows a Mars-van Krevelen-type mechanism over ceria.

The data for pure CeO_2 is also presented in the left panel of Fig. 7 and deviates much from those for CeO_2-like solid solutions. It can be deduced that, even with the same density of surface oxygen vacancies, CeO_2 exhibits a much inferior activity to the CeO_2-like solid solution. This demonstrates that the substitution of Ce by Fe in ceria intrinsically improves the catalytic activity of ceria in CO oxidation, which might be attributed to the lowering of the activation energy of oxygen release in solid solutions. It has been reported that doping ceria with trivalent ions (Pr^{3+} and Tb^{3+}) could lower the activation energy of

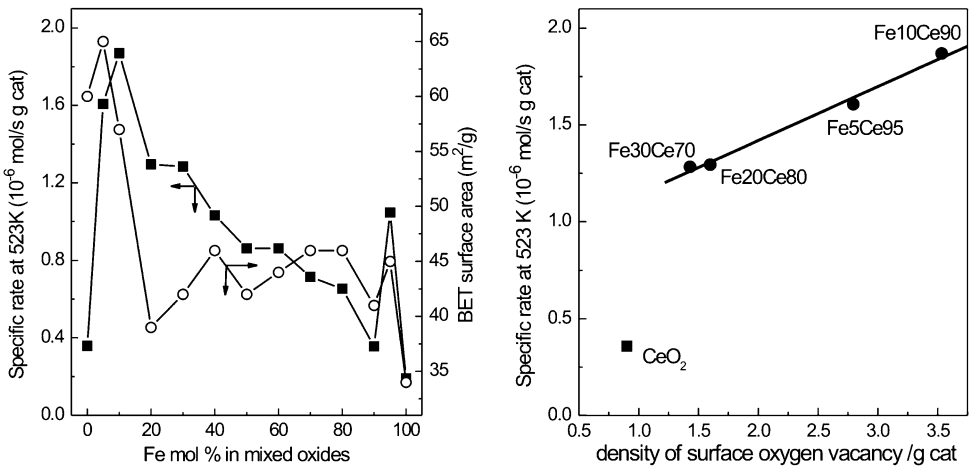

Fig. 7 (left): Specific rates in CO oxidation and specific surface areas of various samples; (right): Specific rates of CeO_2 and CeO_2-like solid solutions in CO conversion as a function of their density of surface oxygen vacancies

oxygen release [17]. The lowering of the activation energy of oxygen release in ceria will definitely enhance its activity in CO oxidation which follows a Mars-van Krevelen-type mechanism. Therefore, ceria-like solid solutions including trivalent ions with a high density of surface oxygen vacancies should be a candidate as an excellent oxide catalyst in CO oxidation.

4 Conclusions

We have investigated the structures of Fe_2O_3–CeO_2 composite synthesized by coprecipitation and also tested their catalytic activity in CO oxidation. The Fe_2O_3–CeO_2 composites form a solid solution with the CeO_2 cubic fluorite structure when the Fe molar percentage was below 0.3, in which the doped Fe^{3+} initially substitutes Ce^{4+} in fluorite cubic CeO_2, but then locates in the interstitial sites after a critical concentration of doped Fe^{3+}. With an Fe molar percentage between 0.3 and 0.95, the Fe_2O_3–CeO_2 composites are mixed oxides of the cubic fluorite CeO_2 solid solution and the hematite Fe_2O_3. CeO_2 is enriched in the surface of Fe_2O_3–CeO_2 composites. The Fe_2O_3–CeO_2 composites have much higher catalytic activity in CO oxidation than the individual pure CeO_2 and Fe_2O_3, and the CeO_2–like Fe10Ce90 solid solution shows the best catalytic performance. Our results establish a proportional relation between the catalytic activity of CeO_2-like solid solutions in CO oxidation and their densities of surface oxygen vacancies, which directly proves the formation of surface oxygen vacancies as the key step in CO oxidation over oxide catalysts.

Acknowledgments This work was financially supported by National Natural Science Foundation of China (grant 20503027), the "Hundred Talent Program" of Chinese Academy of Sciences, the MOE program for PCSIRT (IRT0756), and the MPG-CAS partner group.

References

1. Kăspar J, Fornasiero P (eds) (2002) Catalysis by ceria and related materials. London, Imperial College Press
2. Trovarelli A (1996) Catal Rev Sci Eng 38:439
3. Trovarelli A, de Leitenburg C, Dolcetti G (1997) CHEMTECH 27:32
4. Serre C, Garin F, Maire G (1993) J Catal 141:9
5. Monteiro RS, Dieguez LC, Schmal M (2001) Catal Today 65:77
6. Imamura S, Fukuda I, Ishida S (1988) Ind Eng Chem Res 27:718
7. Mishra VS, Mahajani VV, Joshi JB (1995) Ind Eng Chem Res 34:2
8. Schwartz JM, Schmidt LD (1994) J Catal 148:22
9. Di Monte R, Kaspar J (2004) Top Catal 28:47
10. Mackrodt WC, Fowles M, Morris MA (1991) European Patent 91:165
11. Laachir A, Perrichon V, Badri A, Lamotte J, Catherine E, Lavalley JC, El Fallah J, Hilarie L, Leonormand F, Quemere E, Sauvion GN, Touret O (1991) J Chem Soc Faraday Trans I 87:160
12. Kubsh JE, Rieck JS, Spencer ND (1994) Stud Surf Sci Catal 71:109
13. Fornasiero P, Di Monte R, Ranga Rao G, Kaspar J, Meriani S, Trovarelli A, Graziani M (1995) J Catal 151:168
14. Rynkowski J, Farbotko J, Touroube R, Hilaire L (1995) Appl Catal A 121:81
15. Liu W, Flytzani-Stephanopoulos M (1995) J Catal 153:304
16. Palmqvist AEC, Wirde M, Gelius U, Muhammed M (1999) Nanostruct Mater 11:995
17. Trovarelli A (1999) Comments Inorg Chem 20:263
18. Reddy BM, Khan A, Yamada Y, Kobayashi T, Loridant S, Volta JC (2003) J Phys Chem B 107:11475
19. Monte RD, Kaspar J (2005) J Mater Chem 15:633
20. Reddy BM, Khan A (2005) Catal Surv Jpn 9:155
21. Hrovat M, Holc J, Bernik S, Makovec D (1998) Mater Res Bull 33:1175
22. Tianshu Z, Hing P, Huang H, Kilner J (2001) J Mater Proc Technol 113:463
23. Li G, Smith RI, Inomata H (2001) J Am Chem Soc 123:11091
24. Neri G, Pistone A, Milone C, Galvagno S (2002) Appl Catal B 38:321
25. Kamimura Y, Sato S, Takahashi R, Sodesawa T, Akashi T (2003) Appl Catal A 252:399
26. Pérez-Alonso FJ, López Granados M, Ojeda M, Terreros P, Rojas S, Herranz T, Fierro JLG, Gracia M, Gancedo JR (2005) Chem Mater 17:2329
27. Pérez-Alonso FJ, Mélian-Cabrera I, López Granados M, Kapteijs F, Fierro JLG (2006) J Catal 239:340
28. Machida M, Uto M, Kurogi D, Kijima T (2000) Chem Mater 12:3158
29. Machida M, Kurogi D, Kijima T (2000) Chem Mater 12:3165
30. Dutta G, Waghmare UV, Baidya T, Hegde MS, Priolkar KR, Sarode PR (2006) Chem Mater 18:3249
31. Fang J, Bao HZ, He B, Wang F, Si DJ, Jiang ZQ, Pan ZY, Wei SQ, Huang WX (2007) J Phys Chem C 111:19078
32. Milkes MF, Hayden P, Bhattacharya AK (2003) J Catal 219:295
33. Madier Y, Descorme C, LeGovic AM, Duprez D (1999) J Phys Chem B 103:10999
34. Nibbelke RH, Nievergeld AJL, Hoebnik JHBH, Marin GB (1998) Appl Catal B 19:245
35. Aneggi E, Llorca J, Boaro M, Trovarelli A (2005) J Catal 234:88
36. Moulder TF, Stickle WF, Sobol PE, Bomben KD (1992) Handbook of X-ray photoelectron spectroscopy. Perkin Elmer, Eden Prairie, Minnesota
37. Cornell RM, Schwertmann U (1996) The iron oxides: structure, properties, reactions and uses. VCH Publishers, New York
38. McBride JR, Hass KC, Poindexter BD, Weber WH (1994) J Appl Phys 76:2435
39. De Faria DL, Silva SV, De Oliveira MT (1997) J Raman Spectrosc 28:873
40. Zhang F (2002) Appl Phys Lett 80:127
41. Xie S (2003) J Phys Chem B 105:5144
42. Minervini L, Zacate MO, Grimes RW (1999) Solid State Ionics 116:339
43. Fang J, Bi XZ, Si DJ, Jiang ZQ, Huang WX (2007) Appl Surf Sci 253:8952
44. Burroughs P, Hamnett A, Orchard AF, Thornton G (1976) J Chem Soc Dalton Trans 17:1686
45. Huang WX, Ranke W, Schlögl R (2007) J Phys Chem C 111:2198
46. Praline G, Koel BE, Hance RL, Lee HI, White JM (1980) J Electron Spectrosc Relat Phenom 21:17
47. Kundakovic LJ, Mullins DR, Overbury SH (2000) Surf Sci 457:51